METAL-ORGANIC FRAMEWORKS FOR PRESERVING STRUCTURE AND FUNCTIONALITY OF BIONANOCONJUGATES

A Thesis

by

YIXUAN LI

Submitted to the Office of Graduate and Professional Studies of
Texas A&M University
in partial fulfillment of the requirements for the degree of

MASTER OF SCIENCE

Chair of Committee,	Limei Tian
Committee Members,	Akhilesh Gaharwar
	Daniel Alge
Head of Department,	Michael McShane

August 2020

Major Subject: Biomedical Engineering

ABSTRACT

Nanophotonic biosensors based on plasmonic nanostructures has emerged as a promising platform for molecular diagnostics at the point-of-care. However, poor thermal stability of antibodies and numerous plasmonic nanostructures limit the application of plasmonic biosensors in resource limited settings due to the requirement of cold chain transport. Here, we report the usage of a class of metal-organic framework, zeolitic imidazolate framework-8 (ZIF-8), as a protective coating for the preservation of plasmonic transducers and biorecognition elements. Gold nanobipyramids (AuNBPs) serve as a model plasmonic transducer where sharp geometric features provide improved sensitivity but are prone to reshaping due to its high surface energy. AuNBPs stored at elevated temperatures reveal a rounded tip geometry and reduced sensitivity as plasmonic nanotransducers for localized surface plasmon resonance spectroscopy and surface enhanced Raman spectroscopy. ZIF-8 coating provides AuNBPs and immobilized antibodies with excellent thermal stability with facile synthesis and removal on various substrates. The efficacy, versatility, and facile implementation of ZIF-8 coating offer great promise for the extension of molecular diagnostic serve to resource-limited settings.

DEDICATION

This thesis is dedicated to my father, Mr. Chaoyang Li and my mother, Mrs. Xiaoli Wang. They have been a major source of strength to me throughout my life and inspired me to follow my dreams.

I would also like to dedicate this thesis to my academic advisers and colleagues who mentored and guided me throughout this journey.

ACKNOWLEDGEMENTS

I would like to thank my committee chair, Dr. Limei Tian, for her constant guidance and support and my committee members, Dr. Akhilesh Gaharwar and Dr. Danial Alge for their guidance and support throughout the course of this research. I would also like to thank Dr. Ronald Kaunas, Director of Graduate Programs and Dr. Mike McShane, Head of Biomedical Engineering Department at Texas A&M University for their help and support.

I would also like to thank my colleagues in the Tian lab who have been a major source of support and happiness during my master's at A&M.

Finally, thanks to my mother and father for their encouragement, patience, and support.

CONTRIBUTORS AND FUNDING SOURCES

Contributors

This work was supervised by a thesis committee consisting of Professors Dr. Limei Tian, Dr. Akhilesh Gaharwar and Dr. Daniel Alge of the Department of Biomedical Engineering at Texas A&M University.

All the research work and data contained in the thesis was done by the student. I would like to thank all the members of the Gaharwar lab for their help, useful discussions, and suggestions.

Funding Sources

This work was made possible in part by financial support from the Department of Biomedical Engineering at Texas A&M University, Texas A&M Engineering Experiment Station, and National Science Foundation (Grant No.1648451). The content is solely the responsibility of the author and does not necessarily represent the official views of the funding agency.

NOMENCLATURE

POC	Point-of-Care
LSPR	Localized Surface Plasmon Resonance
LLSPR	Longitudinal Localized Surface Plasmon Resonance
TLSPR	Transverse Localized Surface Plasmon Resonance
RIS	Refractive Index Sensitivity
SERS	Surface Enhanced Raman Spectroscopy
EMF	Electromagnetic Field
AuNBPs	Gold Nanobipyramids
S-AuNBPs	Sharp Gold Nanobipyramids
T-AuNBPs	Truncated Gold Nanobipyramids
MOF	Metal-Organic Framework
ZIF-8	Zeolitic Imidazolate Framework 8
CTAB	Cetyltrimethylammonium Bromide
FDTD	Finite-difference Time-domain
PA	Protein A
IgG	Immunoglobulin G

TABLE OF CONTENTS

Page

ABSTRACT ii

DEDICATION iii

ACKNOWLEDGEMENTS iv

CONTRIBUTORS AND FUNDING SOURCES v

NOMENCLATURE vi

TABLE OF CONTENTS vii

LIST OF FIGURES viii

1. INTRODUCTION AND LITERATURE REVIEW 1

2. MATERIALS AND METHODS 5

2.1. Materials 5
2.2. AuNBPs synthesis 5
2.3. AuNBPs-PA-IgG conjugation 6
2.4. ZIF-8 growth and removal 7
2.5. Finite-Difference Time-Domain (FDTD) Simulation 7
2.6. Surface Enhanced Raman Spectroscopy (SERS) 8
2.7. Characterization 8

3. RESULTS AND DISCUSSION 10

3.1. Characterization of AuNBPs Thermal Reshaping 10
3.2. ZIF-8-mediated structural preservation of AuNBPs 13
3.3. ZIF-8-mediated preservation of AuNBPs performance as SERS substrates 15
3.4. ZIF-8-mediated preservation of AuNBPs refractive index sensitivity 19
3.5. Simultaneous structural and functional preservation of AuNBPs and IgG by ZIF-8 21

4. CONCLUSIONS 26

REFERENCES 27

LIST OF FIGURES

Page

Figure 1 S-AuNBPs reshaping under temperature accelerated storage.....11

Figure 2 AuNBPs reshaping under long term room temperature storage 12

Figure 3. ZIF-8 coating and preservation of S-AuNBPs structure. 14

Figure 4. EM field intensity of S-AuNBPs and T-AuNBPs at 760 nm. 16

Figure 5. Extinction spectrum of S-AuNBPs adsorbed onto laboratory filter paper.....17

Figure 6. SERS performance of AuNBPs, T-AuNBPs and preserved AuNBPs.....18

Figure 7. Refractive index sensitivity of AuNBPs. 20

Figure 8. Incremental shift and specificity of S-AuNBPs following bioconjugation. 22

Figure 9. Simultaneous preservation of AuNBPs and biomolecule by ZIF-8 exoskeleton. 23

Figure 10. TEM image of AuNBPs-PA-IgG following storage at 60°C for 48 hours. 24

1. INTRODUCTION AND LITERATURE REVIEW

Despite significant developments over recent decades, most diagnostic technologies still require centralized clinical laboratories with well-trained technicians and expensive analytical instruments. [1] [2] In resource-limited settings such as low and middle-income countries, battlefields, rural areas, and disaster struck regions, such technologies are remote and inaccessible to the majority of patients and clinicians. [3] [4] Point-of-care (POC) biosensors enables the rapid detection of clinical biomarkers in settings near the patient and away from specialized facilities, thereby minimizing the time and expenditure required for clinical decision making. [5] [6] By some estimates, the extension of laboratory-independent diagnosis into POC settings for tuberculosis, syphilis, malaria, and bacterial pneumonia can prevent 1.2 million deaths annually. [7] [8]

Plasmonic technologies holds enormous potential for the development of a highly sensitive, label-free, and cost-effective biosensor for POC molecular diagnostics. [9] Localized surface plasmon resonance (LSPR) occurs from collective oscillation of conduction electrons in noble metal nanoparticles in response to the oscillating electric field of incident electromagnetic radiation. [10] [11] In the far-field, LSPR result in strong absorption and scattering of incoming electromagnetic radiation which can be measured as a peak in the extinction spectrum. [12] The LSPR extinction maximum is highly sensitive to changes in the local refractive index (RI). [13] Therefore, events such as biomolecular binding that alter the local RI can be directly and rapidly measured without a molecular label. [14] These factors combined with rapid readout and potential for platform

miniaturization has renders LSPR biosensors an attractive option for point-of-care (POC) biosensing. [15]

In the near-field, strong electromagnetic field (EMF) enhancement near the surface of metal nanoparticles has garnered special interest in applications such as surface-enhanced Raman scattering (SERS). [12] [16] Raman scattering occurs when interactions between incident EM radiation and the analyte result in scattered photons that is reduced in energy by the vibrational modes of the analyte molecule. [17] Therefore, spectroscopic analysis based on Raman scattering can identify structurally similar molecules with molecular vibrational fingerprints. [18] However, traditional Raman spectroscopy is hampered by the low scattering intensities (10^{-29} to 10^{-30} cm^2) of Raman scattering. [19] SERS overcomes this shortcoming by recording greatly enhanced Raman signals from analytes adsorbed on a roughened metal surfaces such including metal nanoparticles. [20] EM field enhancement is thought to be the main contributor (~10^4-10^7 fold) to Raman signal enhancement while resonance charge-transfer between the analyte and metal surface is thought to play a lesser role (~10^1-10^2 fold). [21] Highly enhanced sensitivity, narrow spectroscopic bands, and minimal interference from water has enabled SERS to emerge as a powerful analytical tool for trace levels of biological species. [22]

The refractive index sensitivity (RIS) and electromagnetic field (EMF) enhancement of plasmonic nanostructures largely determine the sensitivity of plasmonic biosensors, which are strongly influenced by the size, geometry, and composition of metal nanoparticle transducers.[23] Plasmonic nanostructures with sharp curvatures, such as gold nanobipyramids and nanostars, can provide further improved sensitivity due to a strong

enhancement of electromagnetic fields around their sharp curvatures.[24] However, atoms in these regions tend to undergo structural rearrangements to minimize surface energy, resulting in the poor thermal stability and long-term stability at ambient temperature.[25] Additionally, the analytical validity of biosensors relies on stable biorecognition elements. These biorecognition elements, such as antibodies, are prone to denature when stored at ambient temperature.[26] In the developing world, the ambient temperature can diverge significantly from the required storage temperature. The unreliable supply water and electricity for cold-chain transport severely hamper the reliability of analytical results. [27] [28] These limitations present a significant barrier in the applications of plasmonic sensors for chemical and biological diagnostics. [29] Therefore, there is a critical demand to develop a simple, cost-effective, and biocompatible approach to preserve the structure and functionality of nanoparticles and bionanoconjugates. [30]

Inspired by the natural biomineralization processes in living organisms, metal-organic frameworks (MOFs), composed of metal nodes and organic linkers, have attracted increasing interest as an exoskeleton to protect the biofunctionality of biomolecules.[31] MOF crystals grown around biomolecules form a stable and tight encapsulation layer, thus preventing the structural changes and denaturation.[32] Zeolitic imidazolate framework-8 (ZIF-8) is particularly favored as a class of MOFs due to its large surface area, biocompatibility, excellent thermal and chemical stability, and ease of removal.[31] Exceptional thermal and chemical stability has been demonstrated at temperatures up to 500°C and in organic solvents.[33] ZIF-8 growth occurs spontaneously around biomolecules as proteins, enzymes and nucleic acids accumulate imidazole and inorganic

cations via strong intermolecular hydrogen bonding and hydrophobic interactions.[31] Capping agents used in metal nanoparticle synthesis such as cetyltrimethylammonium bromide (CTAB) also facilitate the interaction between metals surface and ZIF-8 precursors by the hydrophobic tail. [34] To dissolve ZIF-8, aqueous solutions of pH 5.0-6.0 are used to facilitate the on-demand removal by perturbing the coordination between zinc ions and imidazolate.[31] The potency of ZIF-8 to protect biorecognition capability has been demonstrated on human Immunoglobulin G (IgG) conjugated to gold nanorods.[26, 32] The protective capability of ZIF-8 for metal nanomaterials has also been reported by Kang et. al where silver nanowires coated with ZIF-8 is resistant to corrosion, vulcanization, oxidation, and enzymatic degradation. [35] In this paper, we demonstrate that ZIF-8 serves as a versatile nanoexoskeleton to prevent gold nanobipyramids (AuNBPs) from reshaping and to preserve the structure and functionality of bionanoconjugates.

2. MATERIALS AND METHODS

2.1. Materials

Cetyltrimethylammonium bromide (CTAB, ≥99%), gold (III) chloride trihydrate ($HAuCl_4$, ≥99.9%), ascorbic acid (≥99.0%), silver nitrate ($AgNO_3$, ≥99.0%), sodium borohydride ($NaBH_4$, 98%), 8-hydroxyquinoline (8-HQL, 99.0%), poly(sodium-p-styrenesulfonate) (PSS, average M.W. ~1,000,000), and 4-Aminothiophenol (4-ATP, 97%) were purchased from Sigma Aldrich. Nitric Acid (HNO_3, 70%) and sodium hydroxide (NaOH, ≥97.0%) were purchased from Fisher Chemical. Hexadecyltrimethylammonium chloride (CTAC, 99%), 2-methylimidazole (99%) and zinc nitrate (98%) from ACROS Organics. Protein A (PA), human IgG, and goat anti-human IgG were purchased from Invitrogen.

2.2. AuNBPs synthesis

AuNBPs were synthesized following a seed-mediated method with minor modifications. [36] To prepare polycrystalline seeds, 4 ml of $HAuCl_4$ (0.5 mM) and 72 µl of HNO_3 (250 mM) were mixed into an aqueous solution of 4 ml CTAC (95 mM) at room temperature, followed by rapid injection of 100 µl ice-cold mixture containing 50 mM $NaBH_4$ and 50 mM NaOH under vigorous stirring at 1000 rpm. After one minute of stirring, 16 µl of citric acid (1 M) was added and the seed solution was aged in an oil bath at 80°C for 4 hours. The color of the seed solution changed from light yellow to bright

red. Polycrystalline seeds were stored at room temperature prior to use for AuNBPs growth.

AuNBPs growth solution was prepared by adding 36 µl of aqueous $AgNO_3$ (10 mM) and 80 µl of 8-HQL (400 mM in ethanol) into a mixture of 80 µl of aqueous $HAuCl_4$ (25 mM) and 8 ml of aqueous CTAB (47 mM). Following this, 40 µl of polycrystalline seeds was injected to the growth solution, followed by gentle stirring for ten seconds. The growth solution was then placed in an oil bath at 40°C under stirring at 500 rpm. Following 15 minutes of aging, additional 50 µl of 8-HQL (400 mM in ethanol) was injected and the growth solution was aged for another 30 minutes. The color of growth solution changed from light yellow to magenta. Finally, the growth solution was centrifuged once at 7700 rpm for 30 minutes, and redispersed in nanopure water (18.2 mΩ-cm).

2.3. AuNBPs-PA-IgG conjugation

Clean glass substrates were immersed in 0.2 w/v% PSS aqueous solution for 1 hour and rinsed with nanopure water. The PSS-modified glass slides were incubated in AuNBPs solution overnight to achieve uniform adsorption. The AuNBPs coated glass slides were incubated in aqueous PA (10 µg/ml) overnight at 4 °C and rinsed with nanopure water. Subsequently, the AuNBP-PA slides were incubated with human IgG (10 µg/ml in 1X PBS) for 90 minutes, followed by rinsing with 1 ml of 1X PBS and nanopure water. Finally, the AuNBP-PA-IgG slides were incubated with anti-human IgG (10 µg/ml) for 90 minutes, followed by rinsing with 1 ml of 1X PBS and nanopure water. A group

of AuNBP-PA-IgG slides was prepared with additional steps, including ZIF-8 coating, thermal treatment, and removal of ZIF-8 coating prior to incubation with anti-human IgG.

2.4. ZIF-8 growth and removal

ZIF-8 growth solution was prepared based on a previously reported protocol with modifications.[37] Briefly, ZIF-8 growth solution was prepared by mixing 1 ml of aqueous zinc nitrate (24 mM) and 4 µl of CTAB (100 mM) with 2 ml of aqueous 2-methylimidazole (660 mM). The same ZIF-8 growth solution without the addition of CTAB was employed for AuNBP-PA-IgG coated glass slides. The AuNBPs or AuNBP-PA-IgG coated glass slides were incubated in the ZIF-8 growth solution for three hours at room temperature. ZIF-8 coated glass slides were dried with nitrogen gas while TEM grids and paper were naturally dried in air. Following thermal treatment, ZIF-8 coating was removed from AuNBPs or AuNBP-PA-IgG by immersing the substrates in 0.2 M phosphate buffer (pH 5.7) with 2 mM EDTA for two minutes with gentle shaking, followed by rinsing with nanopure water.

2.5. Finite-Difference Time-Domain (FDTD) Simulation

EM field distributions of AuNBPs were calculated using a commercial three-dimensional FDTD software. The absorbing boundary conditions of perfectly matched layer were obtained in different directions. The optical dielectric function of gold is calculated using a Drude–Lorentz dispersion function and the refractive index of the surrounding medium was set to 1 as air in all simulations. Three-dimensional S-AuNBP

and T-AuNBP were calculated based on dimensions measured from TEM images. High-resolution simulation was performed at the excitation wavelength of 780 nm and the emission wavelength of 865 nm to derive the spatial map of EM field intensity enhancement.4

2.6. Surface Enhanced Raman Spectroscopy (SERS)

SERS substrates were prepared by immersing commercially available laboratory paper in AuNBPs solution overnight, followed by rinsing with nanopure water. A group of AuNBP paper was prepared with additional steps, including ZIF-8 coating, thermal treatment, and removal of ZIF-8 coating prior to incubation with p-ATP solution. Subsequently, AuNBPs-coated paper substrates were immersed in various concentration of p-ATP in Ethanol (1 pM, 10 pM, 100 pM, 1 nM, 10 nM, and 100 nM) for 2 hours and thoroughly rinsed with ethanol. Raman spectra were collected from three spots within the same substrate to obtain the average. The spectra were measured in the wavelength range of 400 cm-1-1800 cm-1 with exposure time of 1 s.

2.7. Characterization

UV-Vis spectrophotometer (Shimadzu UV-1900) was used to collect extinction spectra of AuNBPs aqueous solution and AuNBPs on glass slides in the range of 400-1100 nm. Growth of ZIF-8 exoskeleton on AuNBPs was monitored with continuous spectra collection with 2 minutes intervals. Transmission electron microscopy (TEM) images were collected with JEOL 1200 EX and AuNBP dimensions were estimated from

TEM images using ImageJ. Extinction spectra of AuNBPs on paper were measured using a microspectrophotometer (CRAIC 308PV) attached to a Leica optical microscope (DM4M) with 20X objective in the range of 450-900 nm. SERS spectra were measured using a DXR Raman spectrometer with a 780 nm wavelength diode laser (24 mW) as illumination source.

3. RESULTS AND DISCUSSION

3.1. Characterization of AuNBPs Thermal Reshaping

For proof-of-concept, we use AuNBPs as a model plasmonic nanostructure with sharp curvatures to demonstrate the thermal stability of these nanostructures. It is expected that AuNBPs undergo tip truncation to reduce the surface energy as the mobility of surface atoms increase under prolonged exposure to elevated temperatures, as shown in the Figure 1a. AuNBPs were synthesized using a previously reported seed mediated method.[36] Figure 1b shows a transmission electron microscope (TEM) image of as synthesized AuNBPs with 116.7 ± 3.6 nm in length, 33.3 ± 2.0 nm in center width, and sharp tips with the radius of curvature 4.9 ± 0.8 nm, noted as S-AuNBPs. After immobilizing the AuNBPs on glass and TEM substrates, we performed temperature-accelerated stability tests by exposing the samples to a series of thermal treatments, including 125°C or 60°C for different durations of time. After exposure to 125°C for 12 hours, thermally induced structural rearrangement AuNBPs resulted in a shortened structure with truncated tips. We denote the reshaped nanostructures as truncated AuNBPs (T-AuNBPs) (Figure 1b). Corresponding dimension analysis showed the length of S-AuNBPs reduces to 78.1 ± 3.6 nm by ~30.1% (Figure 1c). In contrast, the width of both structures remains similar. The radius of curvature of T-AuNBPs is 11.6 ± 1.4 nm, significantly higher than that of S-AuNBPs, indicating that length reduction is a result of tip truncation with a smoothened curvature (Figure 1c). The aspect ratio (length/width) of S-AuNBPs changes from 3.5 to 2.3.

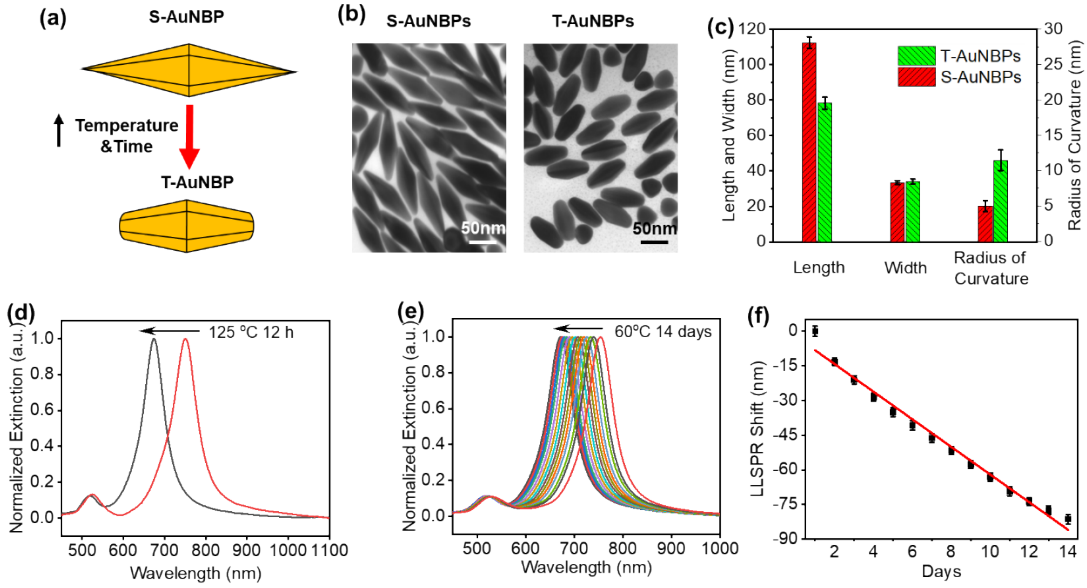

Figure 1 S-AuNBPs reshaping under temperature accelerated storage. (a) Schematic illustration of S-AuNBPs thermal reshaping. (b) TEM images of as-synthesized AuNBPs with sharp tips (AuNBPs) and AuNBPs with truncated tips (T-AuNBPs) after storage at 125°C for 12 hours. (c) Dimension comparison of AuNBPs and T-AuNBPs, measured from (b). (d) Extinction spectra of AuNBPs before and after storage at 125°C for 12 hours. (e) Time evolution of extinction spectra and (f) corresponding LLSPR wavelength shift of AuNBPs after storage at 60°C for 14 days.

The extinction spectrum of S-AuNBPs exhibit two distinct bands with wavelength at 525 nm and 751 nm, corresponding to the transverse and longitudinal oscillation of electrons with incident EM field, respectively. The longitudinal LSPR (LLSPR) band has higher refractive index sensitivity than the transverse LSPR (TLSPR) band. Due to the 125°C treatment, the extinction spectrum of AuNBPs after truncation exhibits a significant blue shift of 78 nm in the LLSPR wavelength from 751 nm to 673 nm and a smaller blue shift of 6 nm in the TLSPR wavelength from 524 nm to 518 nm (Figure 1d). Hereafter,

we use the LLSPR of AuNBPs for analysis due to its higher sensitivity. As expected, exposure to milder condition of thermal treatment at 60°C produces blue shift in the LLSPR wavelength of ~13 nm in the first 24 hours and then with a slower rate of 6 nm blue shift per day (Figure 1e and 1f). The cumulative LLSPR blue shift in S-AuNBPs under 60°C after 13 days reaches a similar extent to that under 125°C after 12 hours.

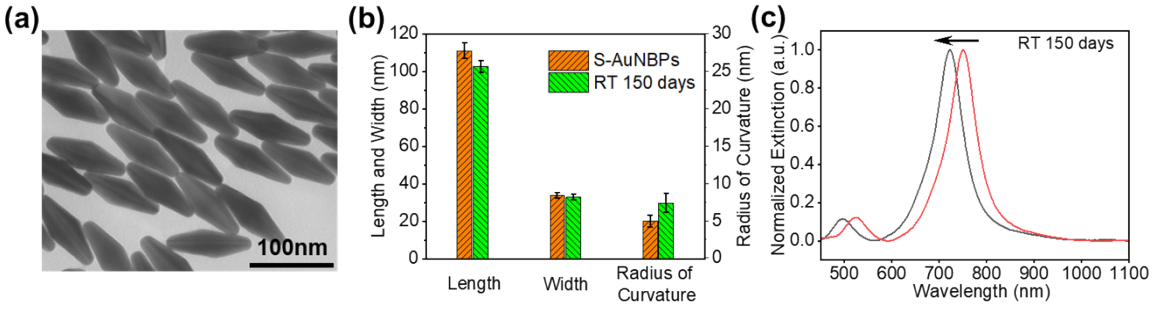

Figure 2 AuNBPs reshaping under long term room temperature storage. (a) TEM images of S-AuNBPs stored at room temperature (RT) for 150 days. (b) Dimension comparison of as S-AuNBPs samples before and after 150 days of storage at RT, measured from (a). (c) Extinction spectra for AuNBPs before and after 150 days of storage at RT.

The prolonged thermal reshaping of AuNBPs under milder conditions is further confirmed by TEM images of AuNBPs showing moderately truncated tips following the storage at room temperature (RT) for 150 days. (Figure 2a). Corresponding dimensional analysis shows that the length of AuNBPs reduces to 102.8 ± 3.1 nm by ~7.6% while the width remains similar (Figure 2b). The radius of curvature of the AuNBPs increased to 7.4 ± 1.3 nm, significantly higher than that of AuNBPs but less than T-AuNBPs exposed to 125°C for 12 hours (Figure 2b). The aspect ratio (length/width) of S-AuNBPs changes from 3.5 to 3.1. Room temperature storage for 150 days produces a blue shift of ~27 nm in the LLSPR wavelength (Figure 2c). These results confirm that the tips of AuNBPs

become truncated and the structural change results in a blue shift in the LSPR wavelength after long-term storage under RT or after exposure to a high temperature for a short time.

3.2. ZIF-8-mediated structural preservation of AuNBPs

To preserve the structure of AuNBPs, we synthesize ZIF-8 nanocrystals around the AuNBPs to suppress the surface diffusion kinetics of the AuNBPs. The formation of ZIF-8 exoskeletons involves the immersion of AuNBPs on substrates to an aqueous solution composed of zinc nitrate (8 mM), 2-methylimidazole (440 mM) and CTAB (0.04 mM) for 3 hours (Figure 3a). The CTAB as an additive facilitates the nucleation and growth of ZIF-8 crystals on metal surfaces, as previously demonstrated. [34, 38] TEM images show a substantial nucleation and growth of ZIF-8 encapsulant around AuNBPs after 5 minutes of immersion in the precursor solution (Figure 3b). The ZIF-8 exoskeleton continues to grow and results in the formation of connected ZIF-8 coating around the AuNBPs following 30 minutes of growth. Time evolution of ZIF-8 crystallization around AuNBPs on glass slides is revealed by measuring the extinction spectra of the AuNBPs immersed in the ZIF-8 precursor solution over time (Figure 3c). The LLSPR wavelength of the AuNBPs after immediately placing in the ZIF-8 precursor solution is measured to be 894 nm. Encapsulation process results in a gradual red shift in the LLSPR wavelength of the AuNBPs with initial rapid growth and gradually plateau over time (Figure 3d). After the growth for 3 hours, the AuNBPs on glass substrates were dried. The ZIF-8 coating results in a red shift of 202 ± 3 nm in LLSPR wavelength of the AuNBPs (Figure 3e).

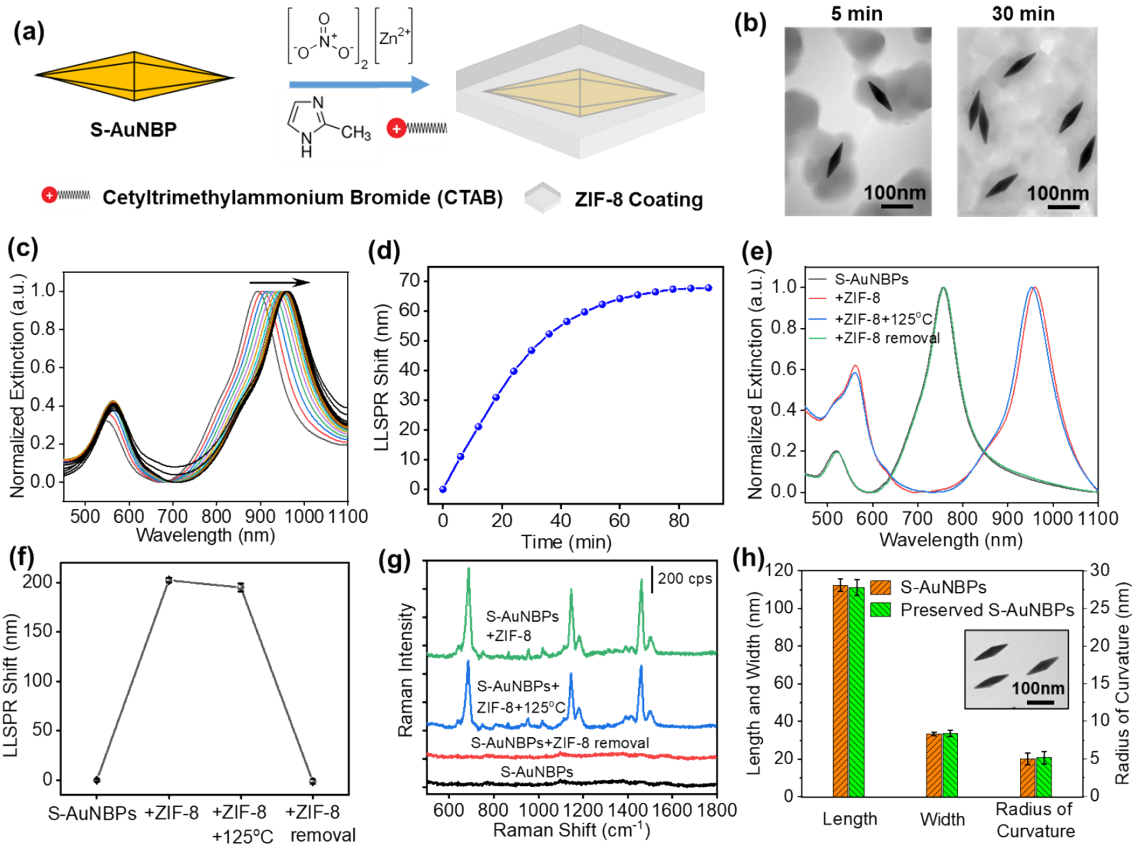

Figure 3. ZIF-8 coating and preservation of S-AuNBPs structure. (a) Schematic illustration of S-AuNBPs encapsulation with ZIF-8 exoskeleton. (b) TEM images of AuNBPs following 5 and 30 minutes of ZIF-8 coating, respectively. (c) Time evolution of the extinction spectra showing the growth of ZIF-8 around AuNBPs and (d) corresponding LLSPR wavelength shift. (e) Extinction spectra of AuNBPs, after ZIF-8 coating, storage at 125°C for 12 hours, and ZIF-8 removal, and (f) corresponding LLSPR wavelength shift following each step, and (g) corresponding Raman spectra following each step. (h) Dimensions of AuNBPs and ZIF-8 preserved AuNBPs. Inset: TEM image of the ZIF-8 preserved AuNBPs.

Next, we demonstrate that ZIF-8 exoskeleton can prevent AuNBPs from reshaping by exposing the ZIF-8 encapsulated AuNBPs under 125°C for 12 hours. The measured extinction spectra show 7 ± 1 nm blue shift in the LLSPR wavelength of ZIF-8 coated AuNBPs due to slight dehydration during the thermal treatment (Figure 3e). We

subsequently removed ZIF-8 coating by immersing the AuNBPs chips in ZIF-8 dissociation buffer composed of 0.2 M phosphate buffer with 2 mM ethylenediaminetetraacetic acid (EDTA) for two minutes followed by rinsing with deionized water. The LLSPR wavelength of the AuNBPs exhibits 196 ± 2 nm blue shift due to ZIF-8 removal (Figure 3e). An additional round of incubation with the dissociation buffer does not result in further blue shift, indicating the complete removal of the ZIF-8 coating. The LLSPR wavelength shows 2 ± 1 nm blue shift compared to the original wavelength of the AuNBPs, suggesting the preservation of the structure (Figure 3f). The coating and removal of ZIF-8 are further confirmed with surface enhanced Raman spectroscopy (SERS). Raman bands at 685 cm^{-1}, 1146 cm^{-1} and 1460 cm^{-1} correspond to the imidazolium ring puckering, C5–N stretching, and antisymmetric methyl bending of ZIF-8, respectively (Figure 3g). [39] The inset image in Figure 2h shows a TEM image of the S-AuBNPs after thermal treatment and ZIF-8 removal and corresponding dimensional analysis of the preserved S-AuBNPs. The dimension of S-AuBNPs preserved with ZIF-8 protective coating does not exhibit any changes compared to the original nanostructures following thermal treatment at 125°C for 12 hours (Figure 3h). These results suggest that ZIF-8 can fully preserve S-AuBNPs structure under high temperature. Rapid coating and on-demand removal of ZIF-8 exoskeleton around nanostructures are also demonstrated.

3.3. ZIF-8-mediated preservation of AuNBPs performance as SERS substrates

SERS is a powerful analytical tool for the quantitative and qualitative measurements of trace amounts of analytes in close proximity to plasmonic nanostructures

with high sensitivity. [40] In SERS based applications, the intensity enhancement of Raman scattering is largely determined by the strong electromagnetic field near the plasmonic nanostructures. [41]. AuNBPs are among a class of anisotropic nanostructures with sharp tips where electromagnetic (EM) field is concentrated to generate EM "hot spots" [42] [43]. Theoretical calculations indicate that AuNBPs exhibit a much stronger EM field enhancement than other nanostructures including nanorods and nanospheres due to the presence of sharp tips [44]. We investigated the EM field enhancement difference between S- AuNBPs and T- AuNBPs with computational and experimental approaches. The finite-difference time-domain (FDTD) simulation calculates the distribution of EM field intensity around S-AuNBPs and T-AuNBPs with the dimension measured from TEM images. The calculated EM field intensity at the excitation wavelength of 780 nm averaged from the area of 30 nm away from the surface of S-AuNBPs is 3.6 times larger than that of T-AuNBPs (Figure 4).

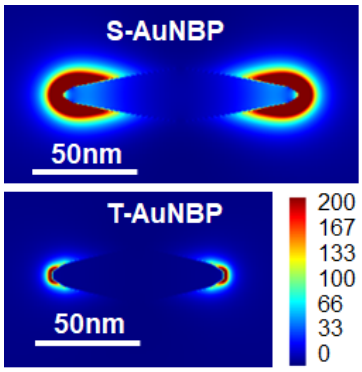

Figure 4. EM field intensity of S-AuNBPs and T-AuNBPs at 760 nm.

We then measured and compared the SERS performance of S-AuNBPs and T-AuNBPs using 4-aminothiophenol (p-ATP) as a model Raman reporter. Following a

previously established approach, AuNBPs uniformly adsorbed on a filter paper serve as a SERS substrate. [45] Extinction spectrum of AuNBPs on paper shows a symmetrical longitudinal band, confirming the uniform distribution of the AuNBPs on the paper substrate (Figure 5).

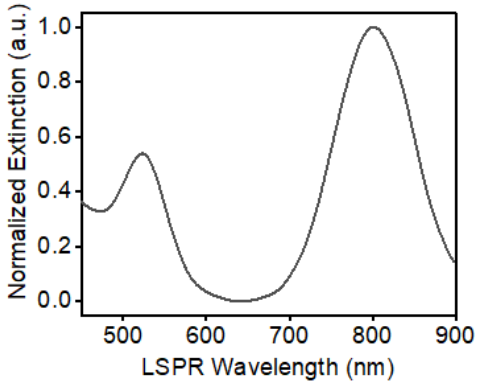

Figure 5. Extinction spectrum of S-AuNBPs adsorbed onto laboratory filter paper.

Following the same approach discussed above, we immerse an S-AuNBPs paper in the ZIF-8 precursor solution for encapsulation, and then expose the paper to the same thermal treatment, followed by the removal of ZIF-8 using the dissociation buffer. Figure 6b and 6c show the SERS spectra of p-ATP adsorbed on the S-AuNBPs and T-AuNBPs after exposure to varying concentrations of p-ATP solution from 100 nM down to 1 pM. The prominent peaks observed at 1140 cm^{-1}, 1390 cm^{-1}, 1436 cm^{-1}, 1574 cm^{-1} correspond to the fundamental benzene ring vibrations (ν_{9b}, ν_3, ν_{19b}, and ν_{8b}, respectively), while the peak at 1072 cm^{-1} corresponds to CS stretching (a_1 mode).[29, 46] As expected, the SERS intensity decreases monotonically with the decrease in the p-ATP concentrations.

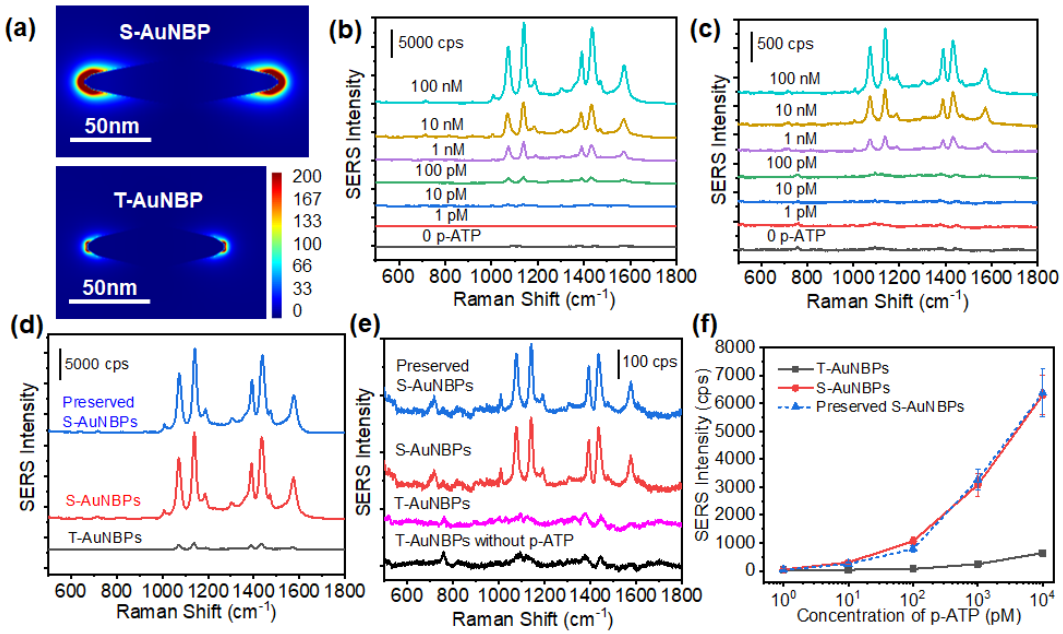

Figure 6. SERS performance of AuNBPs, T-AuNBPs and preserved AuNBPs. (a) EM field intensity of S-AuNBPs and T-AuNBPs at 865 nm. SERS spectra of p-ATP adsorbed on (b) AuNBPs and (c) T-AuNBPs upon exposure to varying concentrations. SERS spectra of p-ATP collected from the T-AuNBPs, S-AuNBPs and preserved S-AuNBPs papers after exposure to (d) 10 nM and (e) 100 pM p-ATP solution, respectively. (f) SERS intensity of 1141 cm−1 Raman band of p-ATP collected from T-AuNBPs, S-AuNBPs and preserved S-AuNBPs papers corresponding to varying concentrations of p-ATP.

Figure 6d shows the SERS spectra of p-ATP collected from the T-AuNBPs, S-AuNBPs and preserved S-AuNBPs papers after exposure to 10 nM p-ATP solutions. The SERS intensities of 1141 cm^{-1} Raman band measured from S-AuNBPs and preserved S-AuNBPs papers are comparable and are ~10 fold higher than that of T-AuNBPs paper. For 780 nm excitation, the Stokes-shift wavelength corresponding to 1141 cm^{-1} Raman band is at ~856 nm. The simulated distribution of EM field intensity around S-AuNBPs at 856 nm is 2.7 times higher than that of T-AuNBPs (Figure 6a). The theoretical SERS enhancement is approximated with the product of the gain in the average EM intensity

enhancement of the incident and Raman scattered light (($|E_{780}|^2|E_{856}|^2$). The calculated SERS enhancement for S-AuNBPs is ~9.7 times larger than that of T-AuNBPs, which agrees well with the higher SERS enhancement of S-AuNBPs in the experimental results. The S-AuNBPs and preserved S-AuNBPs papers allow for the detection of p-ATP at a low concentration of 10 pM (Figure 3e). In contrast, the Raman bands of p-ATP collected from the T-AuNBPs paper at 10 pM are not distinguishable compared to the reference sample without exposure to p-ATP. Figure 3f shows SERS intensity of 1141 cm^{-1} Raman band collected from the T-AuNBPs, S-AuNBPs and preserved S-AuNBPs papers corresponding to the concentrations of p-ATP solutions from 1 pM to 10 nM. The SERS intensity from S-AuNBPs and preserved S-AuNBPs papers follows the same within standard deviation and is higher than that from T-AuNBPs paper at all the concentrations. The low limit of p-ATP detection with S-AuNBPs paper is more than one order magnitude lower than that with T-AuNBPs paper. These results suggest that AuNBPs as SERS nanotransducers provide much higher sensitivity than T-AuNBPs. The ZIF-8 exoskeleton can preserve the structure of AuNBPs used in SERS substrates and the complete removal of ZIF-8 coating does not affect the sensitivity of SERS signals.

3.4. ZIF-8-mediated preservation of AuNBPs refractive index sensitivity

Previous work has shown that shapes and sizes of gold nanocrystals largely affect their refractive index sensitivity (RIS), an important design parameter for LSPR-based sensors. [47] Here, we directly compare the refractive index sensitivity of T-AuNBPs, AuNBPs and preserved AuNBPs. Figure 7a and 7b show the extinction spectra of AuNBPs

and T-AuNBPs after exposing to the concentration of sucrose aqueous solutions from 0% to 42 w/v% to result in a linear increase in refractive index from 1.3333 to 1.4036, respectively. The LLSPR wavelength exhibits gradual red shifts with the increase in the refractive index (Figure 7c). The calculated RIS of the AuNBPs is 353.3 ± 2.4 nm/RIU, which is 29% higher than that of T-AuNBPs (273.5 ± 4.3 nm/RIU). We also prepared ZIF-8 preserved AuNBPs as discussed above. The LLSPR wavelength of the preserved AuNBPs follows the same as that of the AuNBPs with RIS of 351.6 ± 2.8 nm/RIU, further confirming the effective preservation of AuNBPs with the ZIF-8 coating.

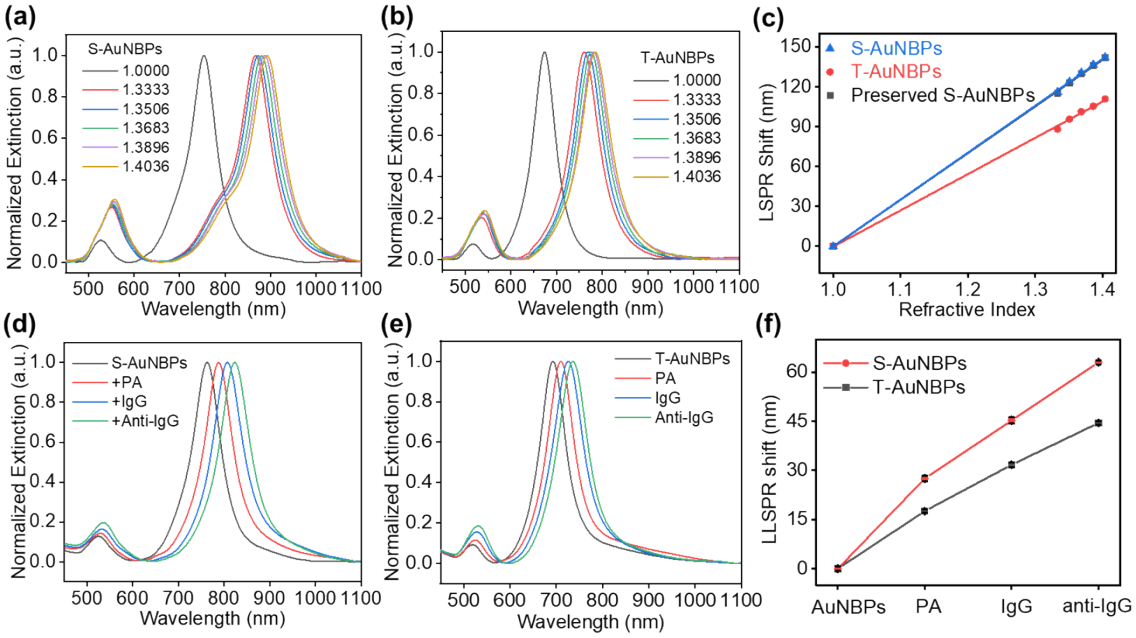

Figure 7. Refractive index sensitivity of AuNBPs. T-AuNBPs and preserved AuNBPs. Extinction spectra of (a) AuNBPs and (b) T-AuNBPs measured in the medium with changing refractive indices, from air to varying concentrations of sucrose aqueous solutions (0-42 w/v%). (c) Corresponding LLSPR wavelength shift and fitted RIS curve for AuNBPs, T-AuNBPs, and Preserved AuNBPs. Extinction spectra of (d) AuNBPs and (e) T-AuNBPs following the conjugation with PA, IgG, and anti-IgG, respectively, and (f) corresponding comparison of LLSPR wavelength shifts of S-AuNBPs and T-AuNBPs after each conjugation step.

We reveal the shape effect of AuNBPs on the sensitivity of LSPR biosensors using human IgG and anti-human IgG as a model pair of biorecognition element and target protein, respectively. First, we functionalize the AuNBPs and T-AuNBPs with Protein A (PA) to conjugate the IgG with a preferable orientation, facilitating the interaction between antigen-binding fragment (Fab) and the target protein. [48] Figure 7d and 7e show the extinction spectra of AuNBPs and T-AuNBPs, following each step of functionalization. The LLSPR wavelength of the AuNBPs exhibits red shift after each step due to the increase in the refractive index (Figure 7f). The LLSPR wavelength shifts of the AuNBPs corresponding to the binding of PA, IgG, and anti-IgG are 27.5 ± 0.8 nm, 17.7 ± 0.9 nm, and 17.8 ± 0.6 nm, respectively. In contrast, the LLSPR wavelength shifts of the T-AuNBPs corresponding to the binding of PA, IgG, and anti-IgG are 17.6 ± 0.5 nm, 14.2 ± 0.7, and 12.7 ± 0.6 nm, respectively. The LLSPR wavelength of the AuNBPs exhibits higher shift than that of the T-AuNBPs for each functionalization step, which agrees well with the higher RIS of the AuNBPs.

3.5. Simultaneous structural and functional preservation of AuNBPs and IgG by ZIF-8

Finally, we demonstrate that the ZIF-8 exoskeleton can simultaneously preserve the S-AuNBPs structure and the functionality of the biorecognition elements for LSPR-based biosensing. AuNBPs-PA-IgG biochips were prepared as described above. We first demonstrated the stability specificity of the AuNBPs-PA-IgG biochip to anti-IgG using S-AuNBPs as substrates. Exposure to 5 mg/ml of bovine serum albumin result in 3.41 ± 0.8

nm redshift of the LLSPR wavelength, significantly less than 17.8 ± 0.6 nm redshift for 10 ug/ml of anti-IgG (Figure 8).

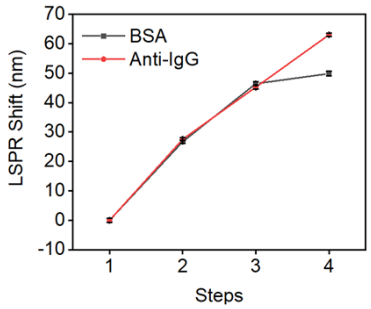

Figure 8. Incremental shift and specificity of S-AuNBPs following bioconjugation.

Figure 9a shows the schematic illustration of ZIF-8 coating around the S-AuNBPs functionalized with PA and IgG, and ZIF-8 removal on demand for anti-IgG detection. The functionalization of the S-AuNBPs with PA and IgG follows the same as the description above. The ZIF-8 coating involves the immersion of the biofunctionalized AuNBPs on glass slides in the ZIF-8 precursor solution composed of zinc nitrate (8 mM) and 2-methylimidazole (440 mM) for 3 hours. No CTAB is added to the ZIF-8 precursor solution as biomolecules are known to facilitate the nucleation and growth of ZIF-8. [31] Time evolution of extinction spectra of AuNBPs-PA-IgG in the ZIF-8 precursor solution shows gradual red shifts in the LLSPR wavelength of the AuNBPs up to ~43 nm at 84 minutes (Figure 9b and 9c). TEM images show a substantial nucleation and growth of ZIF-8 encapsulant around AuNBPs-PA-IgG after 5 minutes of immersion in the precursor solution (Inset image in Figure 5c).

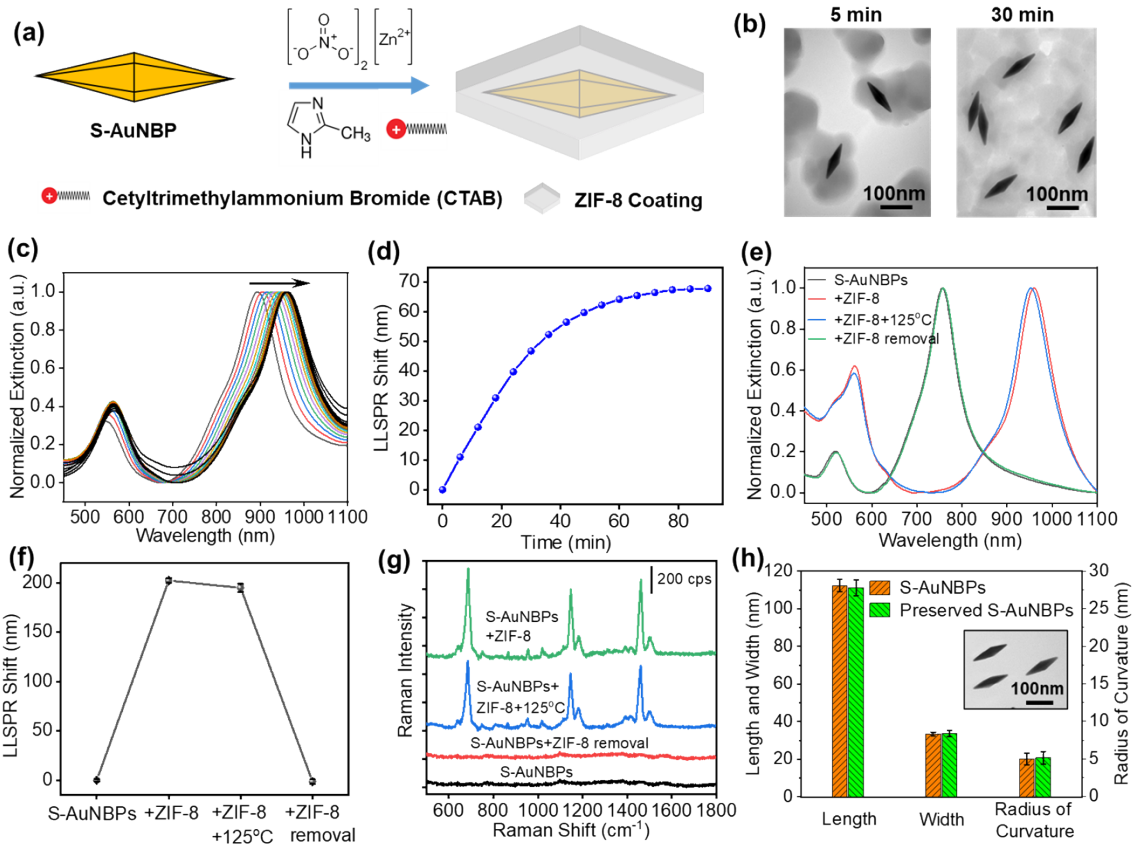

Figure 9. Simultaneous preservation of AuNBPs and biomolecule by ZIF-8 exoskeleton. (a) Schematic illustration of S-AuNBPs-IgG bioconjugation, ZIF-8 coating, ZIF-8 removal, and target (anti-IgG) binding. (b) Time evolution of the extinction spectra showing the growth of ZIF-8 coating around AuNBPs-IgG and (c) corresponding LLSPR wavelength shift. The inset shows a TEM image of AuNBPs-PA-IgG after 5 minutes of ZIF-8 coating. (d) Extinction spectra of S-AuNBPs following each step in (a), and (e) corresponding LLSPR wavelength shift. (f) Extinction spectra of S-AuNBPs, after bioconjuation, storage at 60°C for 48 hours, and anti-IgG binding. (g) Biorecognition retention comparison of S-AuNBPs-PA-IgG with and without ZIF-8 protection.

Figure 9d shows the extinction spectra of the AuNBPs following each step shown in the schematic in the Figure 9a. Figure 9e shows the LLSPR wavelength of the AuNBPs to reveal the incremental LLSPR shift induced by each step. The steps 1-6 represent the fresh AuNBPs, AuNBPs-PA-IgG, ZIF-8 coated AuNBPs-PA-IgG (AuNBPs-PA-

IgG@ZIF-8), AuNBPs-PA-IgG@ZIF-8 after the thermal treatment, AuNBPs-PA-IgG after the ZIF-8 removal, and AuNBPs-PA-IgG after anti-IgG capture, respectively. The LLSPR wavelength of the AuNBPs-PA-IgG exhibits a red shift of 157 ± 2 nm following the ZIF-8 coating. Thermal stability tests involve the exposure of AuNBPs-PA-IgG@ZIF-8 to 60°C for 48 hours. The thermal treatment induces a blue shift of ~7 nm in the LLSPR wavelength of AuNBPs-PA-IgG@ZIF-8 due to dehydration of the ZIF-8. Following the removal of ZIF-8, the LLSPR wavelength of AuNBPs-PA-IgG exhibits a blue shift of ~151 nm and returns to the original wavelength of the AuNBPs-PA-IgG, confirming the complete removal of ZIF-8.

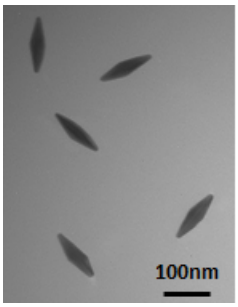

Figure 10. TEM image of AuNBPs-PA-IgG following storage at 60°C for 48 hours.

Subsequently, the binding of the anti-IgG of 10 μg/ml in phosphate-buffered saline (PBS) results in a red shift of 17.5 ± 0.7 nm. For comparison, extinction spectra were collected from to the AuNBPs-PA-IgG without the ZIF-8 protection after the thermal treatment and the anti-IgG binding (Figure 9f). After the thermal treatment, the LLSPR wavelength of AuNBPs-PA-IgG exhibits a blue shift of 17.4 ± 0.5 nm, largely due to the slight truncation of the AuNBPs, confirmed by the TEM image (Figure 10). Upon the

binding of the anti-IgG, the LLSPR wavelength of AuNBPs-PA-IgG shows a red shift of 4.9 ± 0.3 nm without the ZIF-8 protection. The LLSPR wavelength shifts due to the anti-IgG binding are normalized against that measured from the freshly prepared AuNBPs-PA-IgG (17.8 ± 0.6 nm) to derive the percentage retention in biorecognition capability (Figure 9g). The results show 98% biorecognition retention of the ZIF-8 protected AuNBPs-PA-IgG after exposure to 60°C for 48 hours, compared to a retention of only 28% for the unprotected AuNBPs-PA-IgG (Figure 5g). The significant decrease in the biorecognition retention of the unprotected AuNBPs-PA-IgG is attributed to the denaturation of IgG at 60°C. The retention rate of the biorecognition capability with the ZIF-8 demonstrated here is much higher than the reported rate of 80% in previous studies under the same thermal condition. [26] The higher retention is likely due to the better encapsulation by the ZIF-8, evidenced by the higher LSPR wavelength shift of ~157 nm, resulted from the growth of the ZIF, compared to ~65 nm in previous reports. Collectively, we show that the ZIF-8 exoskeleton can preserve the structure and functionality of the AuNBPs-PA-IgG bionanoconjugates.

4. CONCLUSIONS

In conclusion, AuNBPs undergo thermal reshaping at elevated temperatures or after long-time storage at ambient temperature, resulting in the truncation of sharp tips and reduced aspect ratio. The structural change decreases the EM enhancement and RIS of the AuNBPs as nanotransducers. In addition, the biomolecules immobilized on the AuNBPs loose the functionality after the thermal treatment. We demonstrate that ZIF-8 as an exoskeleton can preserve the sharp features of AuNBPs and structure and biofunctionality of bionanoconjugates. The retention of biorecognition capability of antibodies immobilized onto the AuNBPs surface is nearly 100% after two days of storage at 60 °C. This encapsulation approach is applicable to a broad range of nanostructures and bionanoconjugates. The preservation of nanostructures and antibodies can obviate the need for refrigerated transport and storage, suitable for the applications in resource-limited settings.

REFERENCES

[1] P. K. Drain, E. P. Hyle, F. Noubary, K. A. Freedberg, D. Wilson, W. R. Bishai, W. Rodriguez, I. V. Bassett, *The Lancet infectious diseases* **2014**, 14, 239.

[2] C. D. Chin, T. Laksanasopin, Y. K. Cheung, D. Steinmiller, V. Linder, H. Parsa, J. Wang, H. Moore, R. Rouse, G. Umviligihozo, *Nature medicine* **2011**, 17, 1015.

[3] D. Mabey, R. W. Peeling, A. Ustianowski, M. D. Perkins, *Nature Reviews Microbiology* **2004**, 2, 231.

[4] R. Peeling, D. Mabey, *Clinical microbiology and infection* **2010**, 16, 1062.

[5] S. A. Soper, K. Brown, A. Ellington, B. Frazier, G. Garcia-Manero, V. Gau, S. I. Gutman, D. F. Hayes, B. Korte, J. L. Landers, *Biosensors and Bioelectronics* **2006**, 21, 1932.

[6] V. Gubala, L. F. Harris, A. J. Ricco, M. X. Tan, D. E. Williams, *Analytical chemistry* **2012**, 84, 487.

[7] G. J. Kost, *Principles & practice of point-of-care testing*, Lippincott Williams & Wilkins, **2002**.

[8] E. Keeler, M. D. Perkins, P. Small, C. Hanson, S. Reed, J. Cunningham, J. E. Aledort, L. Hillborne, M. E. Rafael, F. Girosi, *Nature* **2006**, 444, 49.

[9] M. Soler, C. S. Huertas, L. M. Lechuga, *Expert review of molecular diagnostics* **2019**, 19, 71.

[10] O. Tokel, F. Inci, U. Demirci, *Chemical reviews* **2014**, 114, 5728.

[11] K. M. Mayer, J. H. Hafner, *Chemical reviews* **2011**, 111, 3828.

[12] C. D. Geddes, *Reviews in Plasmonics 2010*, Springer, **2012**.

[13] J. N. Anker, W. P. Hall, O. Lyandres, N. C. Shah, J. Zhao, R. P. Van Duyne, in *Nanoscience and Technology: A Collection of Reviews from Nature Journals*, World Scientific **2010**, p. 308.

[14] S. Unser, I. Bruzas, J. He, L. Sagle, *Sensors (Basel)* **2015**, 15, 15684.

[15] M.-C. Estevez, M. A. Otte, B. Sepulveda, L. M. Lechuga, *Analytica chimica acta* **2014**, 806, 55.

[16] Q. Min, Y. Pang, D. J. Collins, N. A. Kuklev, K. Gottselig, D. W. Steuerman, R. Gordon, *Optics express* **2011**, 19, 1648.

[17] P. Morris, *Biomedical imaging: applications and advances*, Elsevier, **2014**.

[18] R. Pilot, R. Signorini, C. Durante, L. Orian, M. Bhamidipati, L. Fabris, *Biosensors* **2019**, 9, 57.

[19] M. PROCHAZKA, *SURFACE-ENHANCED RAMAN SPECTROSCOPY: Bioanalytical, Biomolecular and Medical Applications*, SPRINGER, **2017**.

[20] P. Worsfold, A. Townshend, C. F. Poole, M. Miró, *Encyclopedia of analytical science*, Elsevier, **2019**.

[21] P. Jonsson, G. Olofsson, T. Tjärnhage, *Bioaerosol detection technologies*, Springer, **2014**.

[22] F. Li, M. You, S. Li, J. Hu, C. Liu, Y. Gong, H. Yang, F. Xu, *Biotechnology advances* **2020**, 39, 107442.

[23] H. Chen, X. Kou, Z. Yang, W. Ni, J. Wang, *Langmuir* **2008**, 24, 5233.

[24] H. Chen, L. Shao, Q. Li, J. Wang, *Chemical Society Reviews* **2013**, 42, 2679.

[25] A. B. Taylor, A. M. Siddiquee, J. W. Chon, *ACS nano* **2014**, 8, 12071.

[26] C. Wang, L. Wang, S. Tadepalli, J. J. Morrissey, E. D. Kharasch, R. R. Naik, S. Singamaneni, *ACS sensors* **2018**, 3, 342.

[27] S. X. Leng, J. E. McElhaney, J. D. Walston, D. Xie, N. S. Fedarko, G. A. Kuchel, *The Journals of Gerontology Series A: Biological Sciences and Medical Sciences* **2008**, 63, 879.

[28] C. Wang, H. Sun, J. Luan, Q. Jiang, S. Tadepalli, J. J. Morrissey, E. D. Kharasch, S. Singamaneni, *Chemistry of Materials* **2018**, 30, 1291.

[29] A. Abbas, L. Tian, J. J. Morrissey, E. D. Kharasch, S. Singamaneni, **2013**, 23, 1789.

[30] C. Wang, S. Tadepalli, J. Luan, K. K. Liu, J. J. Morrissey, E. D. Kharasch, R. R. Naik, S. Singamaneni, *Advanced Materials* **2017**, 29, 1604433.

[31] K. Liang, R. Ricco, C. M. Doherty, M. J. Styles, S. Bell, N. Kirby, S. Mudie, D. Haylock, A. J. Hill, C. J. Doonan, *Nature communications* **2015**, 6, 7240.

[32] J. Xu, S. H. Wang, G. J. N. Wang, C. X. Zhu, S. C. Luo, L. H. Jin, X. D. Gu, S. C. Chen, V. R. Feig, J. W. F. To, S. Rondeau-Gagne, J. Park, B. C. Schroeder, C. Lu, J. Y. Oh, Y. M. Wang, Y. H. Kim, H. Yan, R. Sinclair, D. S. Zhou, G. Xue, B. Murmann, C. Linder, W. Cai, J. B. H. Tok, J. W. Chung, Z. N. Bao, *Science* **2017**, 355, 59.

[33] G. Lu, O. K. Farha, W. Zhang, F. Huo, J. T. Hupp, *Advanced Materials* **2012**, 24, 3970.

[34] P. Hu, J. Zhuang, L.-Y. Chou, H. K. Lee, X. Y. Ling, Y.-C. Chuang, C.-K. Tsung, *Journal of the American Chemical Society* **2014**, 136, 10561.

[35] H. Kim, H. Jang, J. Moon, J. Byun, J. Jeong, J. Jung, E. K. Lim, T. Kang, *Advanced Materials Interfaces* **2019**, 6, 1900427.

[36] D. Chateau, A. Liotta, F. Vadcard, J. Navarro, F. Chaput, J. Lermé, F. Lerouge, S. Parola, *Nanoscale* **2015**, 7, 1934.

[37] G. Zheng, S. de Marchi, V. López-Puente, K. Sentosun, L. Polavarapu, I. Pérez-Juste, E. H. Hill, S. Bals, L. M. Liz-Marzán, I. Pastoriza-Santos, *Small* **2016**, 12, 3935.

[38] S. Gómez-Graña, F. Hubert, F. Testard, A. Guerrero-Martínez, I. Grillo, L. M. Liz-Marzán, O. Spalla, *Langmuir* **2012**, 28, 1453.

[39] S. Tanaka, K. Fujita, Y. Miyake, M. Miyamoto, Y. Hasegawa, T. Makino, S. Van der Perre, J. Cousin Saint Remi, T. Van Assche, G. V. Baron, *The Journal of Physical Chemistry C* **2015**, 119, 28430.

[40] S. Lin, W. Hasi, X. Lin, S. Han, T. Xiang, S. Liang, L. Wang, *ACS sensors* **2020**, 5, 1465.

[41] J. Lee, J. Seo, D. Kim, S. Shin, S. Lee, C. Mahata, H.-S. Lee, B.-W. Min, T. Lee, *ACS applied materials & interfaces* **2014**, 6, 9053.

[42] H. Xu, J. Aizpurua, M. Käll, P. Apell, *Physical Review E* **2000**, 62, 4318.

[43] M. Liu, P. Guyot-Sionnest, T.-W. Lee, S. K. Gray, *Physical Review B* **2007**, 76, 235428.

[44] H. Dong, T. Lei, F. Yuan, J. Xu, Y. Niu, B. Jiao, Z. Zhang, D. Ding, X. Hou, Z. Wu, *Organic Electronics* **2018**, 60, 1.

[45] a) C. H. Lee, M. E. Hankus, L. Tian, P. M. Pellegrino, S. Singamaneni, *Analytical Chemistry* **2011**, 83, 8953; b) C. H. Lee, L. Tian, S. Singamaneni, *Acs Appl Mater Inter* **2010**, 2, 3429.

[46] a) M. Osawa, N. Matsuda, K. Yoshii, I. Uchida, *The Journal of Physical Chemistry* **1994**, 98, 12702; b) N. Gandra, A. Abbas, L. Tian, S. Singamaneni, *Nano Letters* **2012**, 12, 2645.

[47] a) S. Lee, K. M. Mayer, J. H. Hafner, *Analytical chemistry* **2009**, 81, 4450; b) H. Chen, X. Kou, Z. Yang, W. Ni, J. Wang, *Langmuir* **2008**, 24, 5233; c) H. Chen, L. Shao, K. C. Woo, T. Ming, H.-Q. Lin, J. Wang, *The Journal of Physical Chemistry C* **2009**, 113, 17691.

[48] S. R. Ahmed, A. T. Lutes, T. A. Barbari, *Journal of membrane science* **2006**, 282, 311.